


Enhancing power grid synchronization and stability through time-delayed feedback controlHalgurd Taher,^{1,2} Simona Olmi,^{1,3,*} and Eckehard Schöll²¹*Inria Sophia Antipolis Méditerranée Research Centre, 06902 Valbonne, France*²*Institut für Theoretische Physik, Technische Universität Berlin, 10623 Berlin, Germany*³*CNR, Consiglio Nazionale delle Ricerche, Istituto dei Sistemi Complessi, 50019 Sesto Fiorentino, Italy* (Received 21 January 2019; revised manuscript received 27 May 2019; published 11 December 2019)

We study the synchronization and stability of power grids within the Kuramoto phase oscillator model with inertia with a bimodal natural frequency distribution representing the generators and the loads. The Kuramoto model describes the dynamics of the ac voltage phase and allows for a comprehensive understanding of fundamental network properties capturing the essential dynamical features of a power grid on coarse scales. We identify critical nodes through solitary frequency deviations and Lyapunov vectors corresponding to unstable Lyapunov exponents. To cure dangerous deviations from synchronization we propose time-delayed feedback control, which is an efficient control concept in nonlinear dynamic systems. Different control strategies are tested and compared with respect to the minimum number of controlled nodes required to achieve synchronization and Lyapunov stability. As a proof of principle, this fast-acting control method is demonstrated for different networks (the German and the Italian power transmission grid), operating points, configurations, and models. In particular, an extended version of the Kuramoto model with inertia is considered that includes the voltage dynamics, thus taking into account the interplay of amplitude and phase typical of the electrodynamic behavior of a machine.

DOI: [10.1103/PhysRevE.100.062306](https://doi.org/10.1103/PhysRevE.100.062306)**I. INTRODUCTION**

Synchronization phenomena in nonlinear dynamical networks are of major interest to a wide field of applications in natural and technological systems [1,2], e.g., neural networks in the human brain, or supply and communication networks and power grids, which naturally have a strong link to the economy. Research in these fields has revealed diverse phenomena related to synchronization, ranging from partial synchronization patterns to asynchronous states [3–5]. In particular, scenarios leading from full synchronization to asynchronicity via *solitary* states, i.e., single nodes which are desynchronized from the rest, play an important role for complex dynamical systems [6,7], and in this work we will show that they are fundamental also for power grids.

Infrastructure, e.g., public transportation, medical care, and a vast number of other everyday life applications, rely on electrical power supply. Given the fact that modern power transmission grids, notably if they include renewable energy sources, differ significantly from conventional power grids with regard to topology and local dynamics [8–11], it is necessary to identify, understand, and cure the arising challenges and problems. In particular, malfunctioning grids can be the result of power outages, which occur for various reasons, including line overload or voltage collapse. Here we will focus on the loss of synchrony. In normal operation, a power grid runs in the synchronous state in which all frequencies equal the nominal frequency (50 or 60 Hz) and in which steady power flows balance supply and demand at all nodes. When parts of a power grid desynchronize, destructive power

oscillations emerge. To avoid damage, affected components must then be switched off. However, such switchings can in turn desynchronize other grid components, possibly provoking a cascade of further shut-downs and ending in large area outages of electric supply networks: Recent examples are reported in Refs. [12,13] while extensive studies on large-scale blackout are reported in Refs. [14–17].

The failure of a transmission line during a blackout can be determined not only by the network topology and the static distribution of electric flow but also by the collective transient dynamics of the entire system where the timescale of system instabilities is of seconds [18,19]. In general, grids are designed such that the synchronous state is locally stable, implying that a cascade-triggering desynchronization cannot be caused by a small perturbation. However, even if the synchronous state is stable against small perturbations, the state space of power grids is also populated by numerous stable nonsynchronous states to which the grid might be driven by short circuits, fluctuations in renewable energy generation, or other large perturbations [18,20–22]. Therefore it is of fundamental interest to explore the relation between network properties and grid stability against large perturbations [18,23,24]. Yet many intriguing questions on the relation between grid topology and local stability are still not understood. Decentralized grids tend to be less robust with respect to dynamical perturbations but more robust against structural perturbations to the grid topology [25]. However, adding new links may not only promote but also destroy synchrony, thus inducing power outages when geometric frustration occurs [26,27]. The local stability can be improved by relating the specifics of the dynamical units and the network structure [28–30] or predicting *a priori* which links are critical via the link's redundant capacity and a renormalized response theory [31].

*Corresponding author: simona.olmi@fi.isc.cnr.it

In this paper we will demonstrate the role played by the solitary nodes in driving the populations out of synchrony and the necessity to control these nodes when restoring both stability and synchronization. Solitary nodes can be related to local instabilities via the application of a standard stability toolbox (i.e., Lyapunov exponents and Lyapunov vectors) and to topological properties of the network, like dead ends, thus complementing the analysis reported in Ref. [30]. Once we have identified the critical power grid nodes which undermine stability and synchronization, we will apply time-delayed feedback control to a small subset of these nodes in order to cure a desynchronized and unstable power grid. Time-delayed feedback is an efficient mechanism known in nonlinear dynamics and often used to control unstable systems [32,33]. Generator and consumer dynamics will be described in terms of (i) *Kuramoto oscillators with inertia* [34] and (ii) extended model of Kuramoto rotators with nontrivial voltage dynamics or *synchronous machines* [35]. As a specific example, we consider the topology of the German ultra-high-voltage power transmission grid (220 kV and 380 kV).

II. MODEL AND METHODS

A. The Kuramoto model with inertia

The Kuramoto model with inertia describes the phase and frequency dynamics of N coupled synchronous machines, i.e., generators or consumers within the power grid, where mechanical and electrical phase and frequency are assumed to be identical:

$$\ddot{\theta}_i + \alpha \dot{\theta}_i = \frac{P_i}{I_i \omega_G} + \frac{K}{I_i \omega_G} \sum_{j=1}^N A_{ij} \sin(\theta_j - \theta_i), \quad (1)$$

with the phase $\theta_i(t)$ and frequency $\dot{\theta}_i(t) = \frac{d\theta_i}{dt}$ of node $i = 1, \dots, N$. Both dynamic variables $\theta_i(t)$, $\dot{\theta}_i(t)$ are defined relative to a frame rotating with the reference power line frequency ω_G , e.g., 50 Hz for the European transmission grid. The distribution of net power generation ($P_i > 0$) and consumption ($P_i < 0$) is bimodal; it corresponds to the inherent frequency distribution in the Kuramoto model with rescaled parameters (see Appendix A for a detailed discussion on the parameter selection). The power balance requires $\sum_i P_i = 0$. We assume homogeneously distributed transmission capacities K . The adjacency matrix A_{ij} takes values 1 if node i has a transmission line connected to node j and 0 otherwise. Moreover, α is the dissipation parameter and takes typical values of $0.1-1 \text{ s}^{-1}$ [30,36]. Finally, the moment of inertia I_i of turbine i is $I_i = I = 40 \times 10^3 \text{ kg m}^2$, corresponding to generation capacities of a single power plant equal to 400 MW [30,37]. With the above definitions, the frequency synchronization criterion reads $\dot{\theta}_i(t) = 0$, $\forall i = 1, \dots, N$, i.e., deviations from the reference frequency are zero.

B. Synchronous machine

Equation (1) has been derived in Ref. [34] from the swing equation governing the rotor's mechanical dynamics [36] by assuming constant voltage amplitude and constant mechanical power P_i . The former assumptions make the model incapable of modeling voltage dynamics or the interplay of

amplitude and phase. However, it is possible to extend the model straightforwardly by including the voltage dynamics, thus taking into account the machine's electrodynamic behavior. In the following we consider a lossless network of synchronous machines whose dynamics is described by the extended model derived in Ref. [35]. The coupled dynamics of the phases $\{\theta_i\}$ and magnitudes $\{E_i\}$ of the complex nodal voltages $\{\mathbf{E}_i = E_i e^{i\theta_i}\}_{i \in \{1, \dots, N\}}$ are given by

$$\ddot{\theta}_i + \alpha \dot{\theta}_i = \frac{P_i}{I_i \omega_G} + \frac{K}{I_i \omega_G} \sum_{j=1}^N A_{ij} E_i E_j \sin(\theta_j - \theta_i), \quad (2)$$

$$m_v \dot{E}_i = -E_i + E_{f,i} + X_i \sum_{j=1}^N A_{ij} E_j \cos(\theta_j - \theta_i), \quad (3)$$

where $\dot{\theta}_i$ is the individual frequency of the i th oscillator. P_i denotes the mechanical input or output power and $KA_{ij}E_iE_j \sin(\theta_j - \theta_i)$ is the electrical real power transferred between machines i and j . The susceptance matrix coefficients A_{ij} allow for variations concerning the network topology; as for the previous model, $A_{ij} = 1$ if node i has a transmission line connected to node j and 0 otherwise. In particular the diagonal entries of A_{ij} are chosen such that the matrix has zero row sum $\sum_{i=1}^N A_{ij} = 0$, and m_v , $E_{f,i}$, X_i take into account machine and line parameters. In particular these parameters are set to be homogeneous and of the same order of magnitude as in Ref. [35]: $m_v = 1$, $E_{f,i} = 1$, $X_i = 1$, while the remaining quantities, already discussed in the original model Eq. (1), are chosen as $\alpha = 2 \text{ s}^{-1}$, $I_i = I = 40 \times 10^3 \text{ kg m}^2$, and $\omega_G = 2\pi 50 \text{ Hz}$.

C. German power grid and power distributions

In our numerical example we extract the topology A_{ij} from the *Open Source Electricity Model for Germany* (elmod-de) [38], which describes the German ultra-high-voltage transmission grid using $N = 438$ nodes connected by 662 transmission lines [see Fig. 1(a)].

In many previous studies using the Kuramoto model with inertia to model power grid networks, the distribution of net power generation and consumption P_i is set to be a bimodal δ distribution [25,26,30,39–41]. Here we consider more complex distributions: First, an artificial bimodal Gaussian distribution P^G [42,43] is generated, whose probability density function $p(P)$ is given by the superposition of two Gaussians centered at $\pm P_0$ with standard deviation σ ,

$$p(P) = \frac{1}{2\sigma\sqrt{2\pi}} \left[e^{-\frac{(P-P_0)^2}{2\sigma^2}} + e^{-\frac{(P+P_0)^2}{2\sigma^2}} \right]. \quad (4)$$

Figure 1(b) shows a histogram of the realization P^G used in the numerical simulations of this study. The second distribution P^R shown in Fig. 1(c) is calculated based on data provided by elmod-de [38] and will be referred to as *real-world* distribution.

According to the data documentation [38], elmod-de is an open-source nodal dc load flow model, minimizing generation costs, for the German electric power transmission grid. In the following, we point out how the information in elmod-de is translated into realistic values for the parameters used in our network of Kuramoto oscillators with inertia. As anticipated

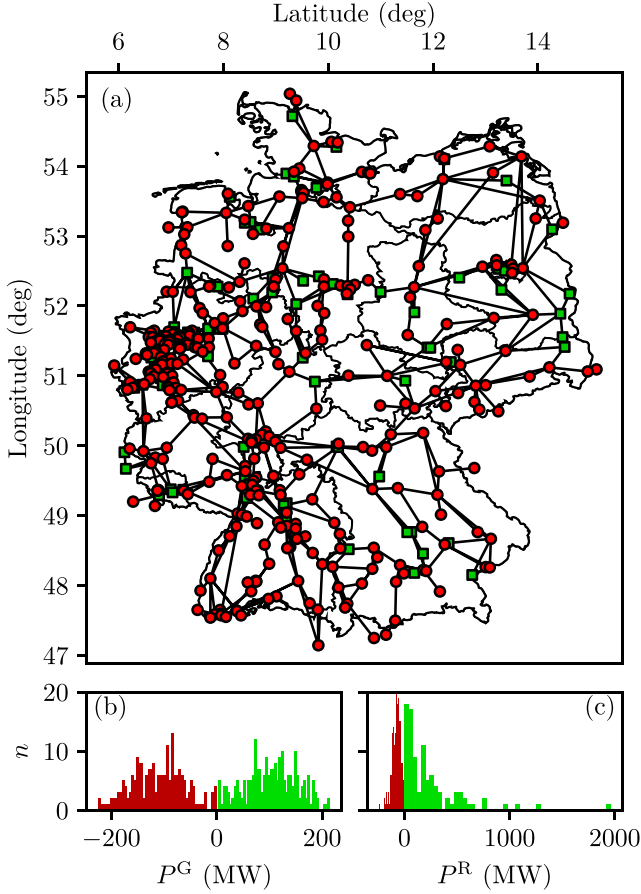


FIG. 1. (a) Map of the German ultra-high-voltage power grid, consisting of 95 net generators (green squares) and 343 net consumers (red dots) connected by 662 transmission lines (black lines). [(b) and (c)] Histograms showing distributions of net power: (b) Realization of an artificial bimodal Gaussian; $P_0 = 105$ MW, $\sigma = P_0/2$. (c) Based on the German power grid. The light green (dark red) bars correspond to generators (consumers). Panels (a) and (c) are constructed from elmod-de data reported in Ref. [38].

above, the data set contains nodal information on $N = 438$ network nodes within the 220-kV and 380-kV ultra-high-voltage transmission grids, of which 393 are substations. The remaining nodes are used to model interactions with neighboring countries (22) and auxiliary nodes (23), e.g., points in the grid without a transformer station. The nodes are connected with 697 transmission lines, 35 of them appearing twice in the data set, which will be neglected, such that 662 unique transmission lines remain. We will furthermore assume identical power transmission capacities for all transmission lines, resulting in a generic coupling strength for the network, thus reducing the values of the coupling matrix to 0 or 1. Besides geographical locations of all nodes, local power demand values p_i are given in parts of the total power demand of Germany at off-peak times:

$$P_{\text{Total}} = \sum_{i=1}^N p_i P_{\text{Total}} = 36 \text{ GW}. \quad (5)$$

Following these definitions the absolute power demand at node $i = 1, \dots, N = 438$ is given by $p_i P_{\text{Total}}$. The spatial

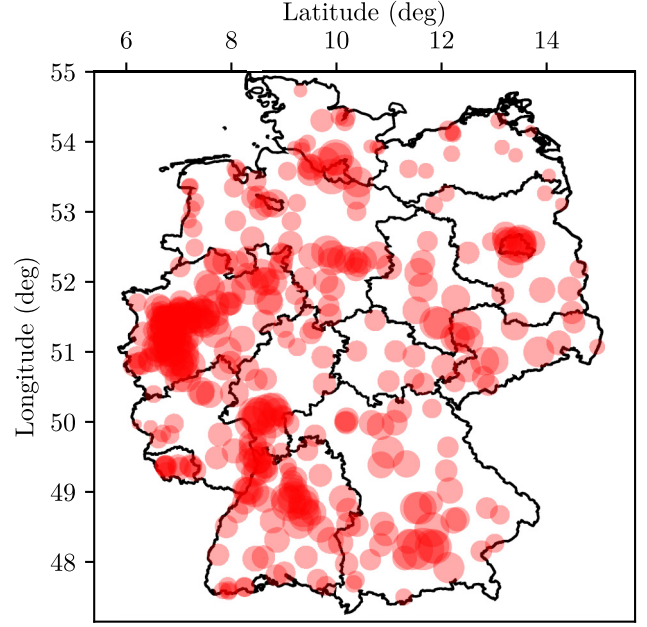


FIG. 2. Spatial distribution of nodal power demands constructed from elmod-de data reported in Ref. [38]. The size of the circles indicate the value of $p_i P_{\text{Total}}$.

distribution of $p_i P_{\text{Total}}$ is illustrated in Fig. 2. Furthermore, 562 conventional power plants, e.g., coal or atomic plants, are listed. Information on the topological location of plants, i.e., to which node i they belong, and their maximum power generation capacities is provided. Let n_i be the number of power plants associated with node i . The maximum capacity of plant $k = 1, \dots, n_i$ located at node i will be denoted by C_i^k . In order to obtain nodewise generation capacities C_i , C_i^k will be aggregated for each node:

$$C_i = \begin{cases} \sum_{k=1}^{n_i} C_i^k & n_i > 0 \\ 0 & n_i = 0 \end{cases}. \quad (6)$$

The spatial distribution of C_i is illustrated in Fig. 3. The total generation capacity C_{Total} reads:

$$C_{\text{Total}} = \sum_{i=1}^N C_i = 88.354 \text{ GW}. \quad (7)$$

Due to the fact that plants being operated at 100% of their maximum generation capacities would cause a large oversupply of power generation and break power balance, we will assume each plant to be operated at 41% of its maximum capacity, since $P_{\text{Total}}/C_{\text{Total}} \approx 0.41$. With this intermediate level of power generation, the power balance is fulfilled and the net generation or consumption P_i at node i is given by:

$$P_i = 0.41 C_i - p_i P_{\text{Total}}. \quad (8)$$

D. Macroscopic indicators and Lyapunov analysis

We consider a scenario where, due to an arbitrary dynamical perturbation, some critical nodes have become desynchronized, where we define as critical those nodes withstanding self-organized resynchronization. Synchronization is

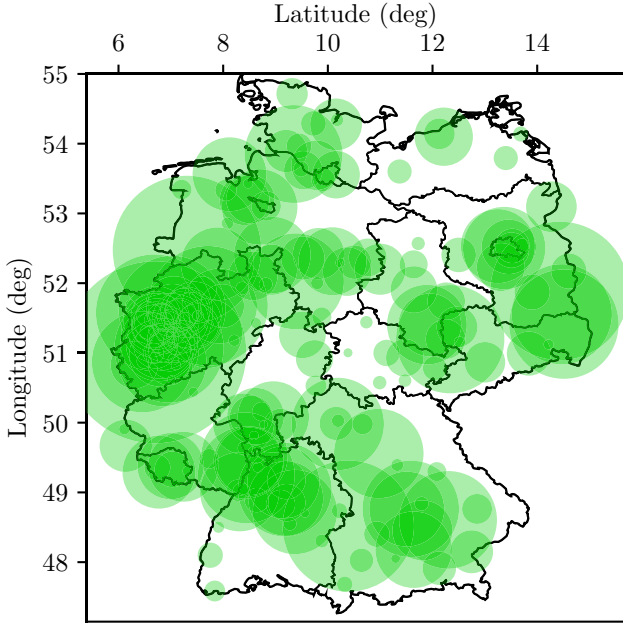


FIG. 3. Spatial distribution of nodal generation capacities constructed from elmod-de data reported in Ref. [38]. The size of the circles indicate the value of C_i .

first gained by performing an adiabatic transition from the asynchronous to the synchronized state for increasing coupling constant: Starting with random initial conditions $\theta_i(0) \in [-2\pi, 2\pi)$, $\dot{\theta}_i(0) \in [-1, 1)$ at $K = 0$, the coupling strength K is increased adiabatically up to K_{Max} , where the system shows synchronized behavior. For each investigated value of K , the system is initialized with the final conditions found for the previous coupling value, and then the system evolves for a transient time T_A , such that it can reach a steady state. After the transient time T_A , characteristic measures are calculated in order to assess the quality of synchronization and the stability of the underlying state $\{\theta_i(T_A), \dot{\theta}_i(T_A)\}$. In particular the time-averaged phase velocity profile $\langle \omega_i \rangle_t \equiv \langle \dot{\theta}_i \rangle_t$ provides information on frequency synchronization of individual nodes i , whereas the standard deviation of frequencies

$$\Delta\omega(t) \equiv \frac{1}{N} \sqrt{\sum_{i=1}^N [\omega_i(t) - \bar{\omega}(t)]^2} \quad (9)$$

is used to estimate the deviation from complete frequency synchronization [$\bar{\omega}(t)$ indicates the instantaneous average grid frequency].

Once a desired synchronized state is reached, a perturbation can occur leading the state out of synchrony. In this situation the overall stability of the power grid might be lost, and therefore it is necessary to analyze the time evolution of small dynamic perturbations $\delta\theta_i := \theta_i^* - \theta_i$ around the steady state θ_i^* , whose dynamics is ruled by the linearization of Eq. (1) as follows:

$$\delta\ddot{\theta}_i + \alpha\delta\dot{\theta}_i = \frac{K}{I\omega_G} \sum_{j=1}^N A_{ij} \cos(\theta_j - \theta_i)(\delta\theta_j - \delta\theta_i). \quad (10)$$

For the extended model, the linearization of Eqs. (2) and (3) reads as

$$\delta\ddot{\theta}_i + \alpha\delta\dot{\theta}_i = \frac{K}{I\omega_G} \sum_{j=1}^N A_{ij} [E_i E_j \cos(\theta_j - \theta_i)(\delta\theta_j - \delta\theta_i) + (\delta E_i E_j + E_i \delta E_j) \sin(\theta_j - \theta_i)] \quad (11)$$

$$m_v \delta\dot{E}_i = -\delta E_i + X_i \sum_{j=1}^N A_{ij} [-E_j \sin(\theta_j - \theta_i)(\delta\theta_j - \delta\theta_i) + \delta E_j \cos(\theta_j - \theta_i)]. \quad (12)$$

The exponential growth rates of the infinitesimal perturbations are measured in term of the associated Lyapunov spectrum $\{\lambda_k\}$, with $k = 1, \dots, 2N$, numerically estimated by employing the method developed by Benettin *et al.* [44]. In particular one should consider for each Lyapunov exponent λ_k the corresponding $2N$ -dimensional tangent vector $\mathcal{T}^{(k)} = (\delta\theta_1, \dots, \delta\theta_N, \delta\theta_1, \dots, \delta\theta_N)$ whose time evolution is given by Eq. (10) [respectively, Eqs. (11) and (12) for the extended model]. Important information about the sources of instability, and, in particular, about the oscillators that are more actively contributing to the chaotic dynamics, can be gained by calculating the time-averaged evolution of the tangent vector $\mathcal{T}^{(1)}$, here referred to as maximum Lyapunov vector. The Euclidean norm of each $\{\theta_i, \dot{\theta}_i\}$ pair in $\mathcal{T}^{(1)}$, averaged in time, is measured for each oscillator as $\xi_i := \langle \sqrt{[\delta\theta_i(t)]^2 + [\delta\dot{\theta}_i(t)]^2} \rangle_t$, once the tangent vector is orthonormalized, i.e., $\|\mathcal{T}^{(1)}\| = 1$.

E. Time-delayed feedback control

In order to enhance frequency synchronization and stability when the system is subject to a dynamical perturbation, the Kuramoto model with inertia is extended by time-delayed feedback control which is an efficient control concept, well known in nonlinear dynamic systems [32,33] but not commonly employed in power grid engineering [45–47]:

$$\ddot{\theta}_i + \alpha\dot{\theta}_i = \frac{P_i}{I\omega_G} + \frac{K}{I\omega_G} \sum_{j=1}^N A_{ij} \sin(\theta_j - \theta_i) - \frac{g_i \alpha}{\tau} [\theta_i(t) - \theta_i(t - \tau)], \quad (13)$$

where g_i is the control gain of node i and τ is the delay time. While primary control sets in to stabilize the frequency and to prevent a large drop within few seconds after a shortage, secondary control is necessary to restore the frequency back to its nominal value of 50 or 60 Hertz within few minutes. On the other hand, our delayed feedback control is able both to stabilize the frequency of the power plant at the origin of the perturbation and to restore the frequency back to its nominal value within few seconds.

Equivalently, for the extended model, the introduction of time-delayed feedback control reads

$$\ddot{\theta}_i + \alpha\dot{\theta}_i = \frac{P_i}{I_i \omega_G} + \frac{K}{I_i \omega_G} \sum_{j=1}^N A_{ij} E_i E_j \sin(\theta_j - \theta_i) - \frac{g_i \alpha}{\tau} [\theta_i(t) - \theta_i(t - \tau)],$$

$$m_v \dot{E}_i = -E_i + E_{f,i} + X_i \sum_{j=1}^N A_{ij} E_j \cos(\theta_j - \theta_i). \quad (14)$$

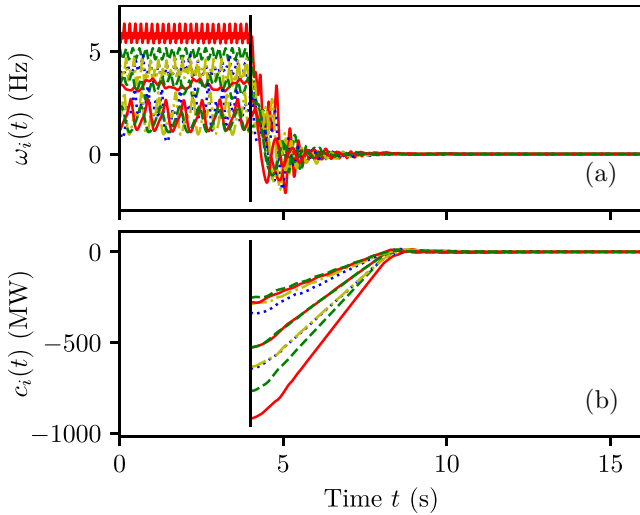


FIG. 4. Power characteristics of time-delayed feedback using the extended model and the German grid with P^R : (a) Frequencies $\omega_i(t)$ and (b) control powers c_i of controlled solitary nodes versus time t . The vertical line indicates the onset of control. The set of controlled nodes ($N_c = 10$) is chosen according to the strategy shown in Fig. 14(b). Delay time $\tau = 4$ s. The feedback gain g_i is set to $g_i = 1.3$ for controlled nodes and $g_i = 0$ for other nodes. Parameters: $m_v = 1$, $E_{f,i} = 1$, $X_i = 1$, $K = 1307$ MW, $\alpha = 2$ s $^{-1}$, $I_i = I = 40 \times 10^3$ kg m 2 , $\omega_G = 2\pi 50$ Hz.

For both models it turns out that the control is robust against changes in the parameters τ, g_i , as shown in Appendix A. In particular, control performance at large enough gain is comparable for a wide range of delay times, therefore, without loss of generality we have chosen $\tau = 4$ and $g = 1$, where the chosen delay time lies within that range. The control term introduced in Eq. (13) [and equivalently in (14)], i.e., $\frac{1}{\tau}[\theta_i(t) - \theta_i(t - \tau)]$, represents a running frequency average:

$$\langle \omega_i \rangle_t := \frac{1}{\tau} \int_{t-\tau}^t \dot{\theta}_i(t') dt' = \frac{1}{\tau} [\theta_i(t) - \theta_i(t - \tau)], \quad (15)$$

where phases are measured cumulatively. Since in the Kuramoto model with inertia only phase differences are important for the dynamics, we do not require phases to be in $[0, 2\pi]$ (or $[-\pi, \pi]$).

Moreover, the control strength that we use is realistic (e.g., ≈ 900 MW for a single node at the onset of control for the setup shown in Fig. 14) and within the order of magnitude of power characteristic requirements reported in Ref. [48]. Details of the power characteristics are given in Fig. 4 for the extended model with voltage dynamics [Eqs. (14)], simulated on the German high-voltage grid, with real-world natural frequency distribution. In particular the control power, reported in Fig. 4(b), is defined as

$$c_i(t) := -\frac{g_i \alpha I \omega_G}{\tau} [\theta_i(t) - \theta_i(t - \tau)]. \quad (16)$$

In our simulations the power c_i of controlled nodes does not exceed the maximum control power treatable by frequency primary control in Germany (data for frequency and volt-

age control ancillary services in Germany are reported in Ref. [48]).

Finally, it is worth highlighting that the control scheme is applied to a subset of nodes, chosen according to suitably designed strategies. The possibility to control few nodes out of a big network makes the stabilization of the network faster: The control in principle can be switched on for all emerging critical nodes and it turns off automatically when the node is synchronized again. Since the control vanishes at full synchronization, it does not double the dissipation rate permanently.

III. RESULTS FOR A NETWORK OF KURAMOTO OSCILLATORS WITH INERTIA

A. Emergence of solitary states

In general we have performed sequences of simulations by varying adiabatically the coupling parameter K with two different protocols. Namely, for the upswEEP protocol, as described in the previous section, the series of simulations is initialized for the decoupled system by considering random initial conditions both for phases and frequencies. Afterward the coupling is increased in steps of ΔK until a maximum coupling strength K_{Max} is reached. For the downswEEP protocol, starting from the maximum coupling strength K_{Max} achieved by employing the upswEEP protocol simulation, the coupling is reduced in steps of ΔK until $K = 0$ is recovered. At each step the system is simulated for a transient time T_A followed by a time interval T_W during which the average frequencies $\langle \omega_i \rangle_t$, as well as the components of the Lyapunov vector ξ_i and the maximum Lyapunov exponent λ_1 , are calculated. An example of the results obtained by performing the sequence of simulations of upswEEP followed by downswEEP is shown in Figs. 5 and 6 for the bimodal Gaussian distribution P^G and the real-world distribution P^R , respectively.

In both cases, at low coupling, a large fraction of the network is unsynchronized [Figs. 5(a) and 6(a)] and the system is chaotic, i.e., $\lambda_1 > 0$ [Figs. 5(b) and 6(b)]. A considerable part of the oscillators rotates with average frequency $|\langle \omega_i \rangle| > 0$, while relatively few oscillators are locked at average zero frequency [Figs. 5(c) and 6(c)]. Other clusters at $|\langle \omega_i \rangle| \neq 0$ may emerge. The *solitary nodes*, which are desynchronized from the rest of the network, and oscillate with high frequency, are those mostly responsible for the lack of synchronization. This is revealed by the analysis of the components of the maximum Lyapunov vector ξ_i , which assume large values for those nodes which are solitary, thus indicating that the directions identified by solitary nodes are the most unstable in the network [as shown in Figs. 5(f) and 6(f)].

For intermediate K values, the majority of nodes is synchronized on average, with a small set of nodes being solitary, for instance, 9 for the Gaussian and 11 for the real-world distribution [see Figs. 5(a) and 6(a) and then Figs. 5(d) and 6(d)]. The system is still chaotic [Figs. 5(b) and 6(b)] and the components of the Lyapunov vector ξ_i are still localized around solitary nodes [Figs. 5(g) and 6(g)]. The number of solitary nodes diminishes for increasing coupling values, since more and more nodes join the main synchronized cluster at zero average frequency. Just before full synchronization

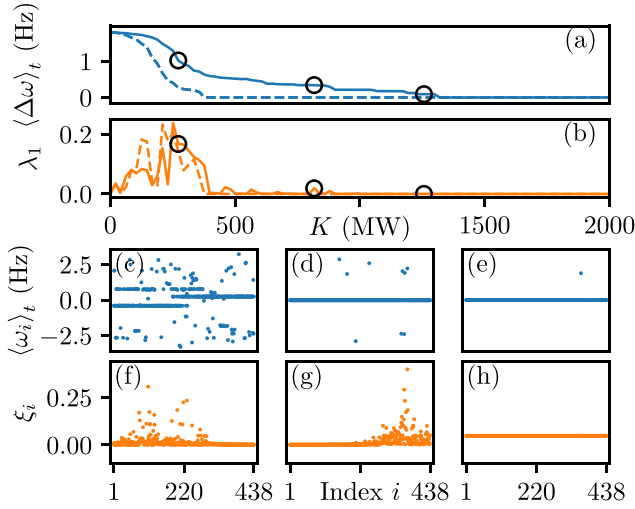


FIG. 5. German power grid with bimodal Gaussian distribution P^G : (a) Average frequency deviation $\langle \Delta\omega \rangle_t$ and (b) largest Lyapunov exponent λ_1 versus coupling strength K . The solid (dashed) lines correspond to the adiabatic upswep (downsweep) of K . [(c)–(e)] Average frequencies $\langle \omega_i \rangle_t$ and [(f)–(h)] Lyapunov vector components ξ_i versus node index i for the K values marked by black circles in the top panels from left to right. Parameters: $0 \leq K \leq 3142$ MW in steps of $\Delta K \approx 21$ MW with $\alpha = 5/6$ s $^{-1}$, $I_i = I = 40 \times 10^3$ kg m 2 , $\omega_G = 2\pi 50$ Hz. Averages taken over 100 s after discarding a transient time of 400 s. Lyapunov exponents and vectors calculated for a duration of 4×10^5 s. Lyapunov exponents are expressed in units of $\Delta t^{-1} = 5$ s $^{-1}$.

[see Figs. 5(e) and 6(e)], one solitary node is left and no instability emerges in the system [Figs. 5(h) and 6(h)]. The fully synchronized state ($\langle \Delta\omega \rangle_t = 0$) is stable and it is characterized by a single cluster with no solitary nodes. In particular complete frequency synchronization with $\langle \Delta\omega \rangle_t = 0$, $\lambda_1 = 0$ is achieved at $K \geq 1320$ MW ($K \geq 4200$ MW) for P^G (P^R).

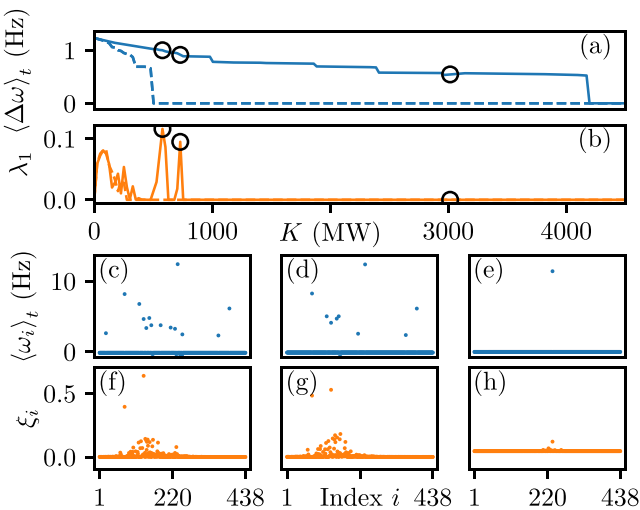


FIG. 6. German power grid with real-world distribution P^R : Same as in Fig. 5. Parameters: $0 \leq K \leq 4500$ MW in steps of $\Delta K \approx 25$ MW with $\alpha = 2$ s $^{-1}$. Other parameters as in Fig. 5.

When K is decreased starting from the synchronized states, the system remains synchronized for a larger K interval, due to the hysteretic nature of the transition, and the synchronized state loses stability (i.e., $\langle \Delta\omega \rangle_t > 0$) for a coupling value smaller than the one found during the upswep protocol [see Figs. 5(a) and 6(a)]. The system is multistable and partially synchronized states [as those shown in Figs. 5(d) and 6(d)] coexist with the synchronized one. Depending on the initial state of the system, the dynamics can approach either the synchronized state or one of the upper branch states. This also means, that, starting from the synchronized states, large perturbations can kick the system out of synchrony. In order to visualize this scenario in terms of running power grids, we can resort to the infinite bus model, commonly used in engineering literature to analyze the return to synchrony after a frequency perturbation at a node: The standard analysis neglects the back-reaction of the dynamics at node i on the other nodes and keeps them fixed, i.e., $\ddot{\theta}_i + \alpha \dot{\theta}_i = \frac{P_i - K \sin(\theta_i)}{I_i \omega_G}$. When decoupling this system ($K = 0$) the oscillator rotates freely with frequency $P_i/(\alpha I_i \omega_G)$. When the coupling is switched on, this limit cycle persists, and in the absence of losses its average frequency stays close to $P_i/(\alpha I_i \omega_G)$. This might be seen as a simple model for solitary states, where the infinite bus represents the remaining synchronous component. If they occur in a running grid, the solitary nodes are normally switched off as soon as their frequency falls outside a certain range around the nominal value.

The goal of this paper is to give a proof of principle that once such a partially synchronized state is approached, our control method is capable of synchronizing and stabilizing the system. Thus in the following we consider the two unstable states present in Figs. 5(d), 5(g) and Figs. 6(d), 6(g), which we aim to control.

B. Application of time-delayed feedback control

To facilitate understanding we report in Fig. 7 the main features of the unstable states, briefly introduced in the previous section, that we aim to control. In particular Fig. 7 shows the time-averaged standard frequency deviation $\langle \Delta\omega \rangle_t$ and the maximum Lyapunov exponent λ_1 for each value K of the adiabatic increase for the bimodal Gaussian [Fig. 7(a)] and for the real-world distribution [Fig. 7(b)] and highlights the considered operating points via dashed black lines.

If a perturbation pushes the system out of synchrony at an intermediate state with finite values of $\langle \Delta\omega \rangle_t$, in a chaotic regime characterized by $\lambda_1 > 0$, then would it be possible to enhance synchronization and stability by controlling a small subset of nodes? In the following we will give a positive answer to this question by exploring the dynamics of the system at $K \approx 817$ MW ($K \approx 729$ MW) for P^G (P^R), where deterministic chaos is present, i.e., $\lambda_1 = 0.0187$ ($\lambda_1 = 0.096$), and the system is not perfectly frequency synchronized: $\langle \Delta\omega \rangle_t \approx 0.34$ Hz ($\langle \Delta\omega \rangle_t \approx 0.91$ Hz), modeling a strongly perturbed power grid [49]. Even though we are considering a partially synchronized regime with an intermediate transmission capacity value, as a resulting regime in case of strongly perturbed grid, we made sure not to artificially drive the system to an unrealistic range of capacity values. Indeed, the operating point at which we are working is in a realistic

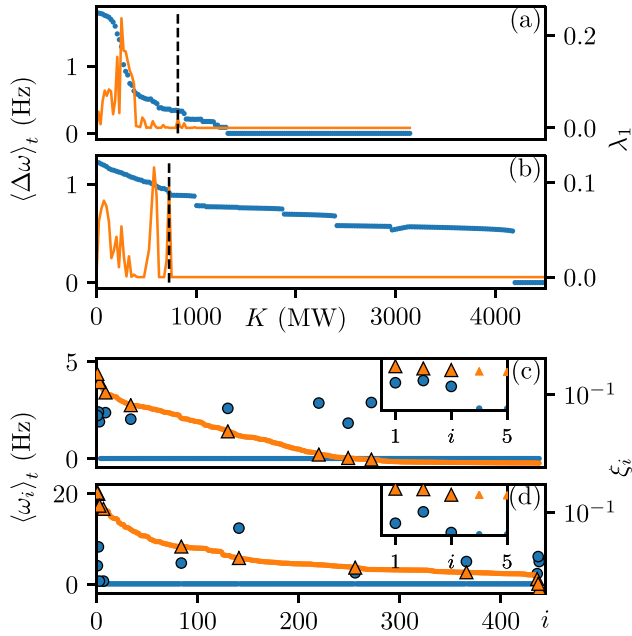


FIG. 7. Time-averaged standard frequency deviation $\langle \Delta\omega \rangle_t$ (blue dots) and maximum Lyapunov exponent λ_1 (orange line) versus coupling strength K for the bimodal Gaussian P^G (a) and for the real-world distribution P^R (b), calculated for the upswep protocol. The dashed black lines highlight the operating K points. Time-averaged phase velocity profile $\langle \omega_i \rangle_t$ (dark blue dots) and Lyapunov vector components ξ_i (light orange triangles) versus node index i for the bimodal Gaussian at $K \approx 817$ MW (c) and for the real-world distribution at $K \approx 729$ MW (d). Data are ordered in descending order of ξ_i . The insets show a zoom for small i . Large circles (triangles) mark $\langle \omega_i \rangle_t$ (ξ_i) of solitary nodes. For P^G $0 \leq K \leq 3142$ MW in steps of $\Delta K \approx 21$ MW with $\alpha = 5/6 \text{ s}^{-1}$. For P^R $0 \leq K \leq 4500$ MW in steps of $\Delta K \approx 25$ MW with $\alpha = 2 \text{ s}^{-1}$ [50]. Other parameters as in Fig. 5.

regime when considering the average transmission capacity (≈ 1500 MW) at which the German ultra-high-voltage transmission grid works, according to the elmod-de data set.

From the average frequency profile shown in Fig. 7(c) [Fig. 7(d)] for P^G (P^R), we can see that a major part of the power grid is frequency synchronized while few nodes have a significant frequency deviation and are identified as *solitary states*: nine nodes for P^G and 11 nodes for P^R . (Note that the three solitary nodes $i = 1, 2, 3$ can only be resolved in the blown-up inset.) Solitary nodes oscillate with their own average frequency and do not resynchronize in a self-organized way at a given coupling strength, being thus critical for desynchronization. Note that the solitary nodes include those with the largest ξ_i but not only those.

In order to enhance frequency synchronization and stability at the intermediate coupling strength discussed above, we introduce time-delayed feedback control as in Eq. (13). The *modus operandi* of the control method is shown in Fig. 8, where all solitary states are controlled for both natural frequency distributions, P^G and P^R . In particular Fig. 8(a) [Fig. 8(b)] shows the instantaneous deviation $\Delta\omega(t)$ before and after the control is activated in presence of P^G (P^R) for the set of controlled nodes. In approximation, the deviation

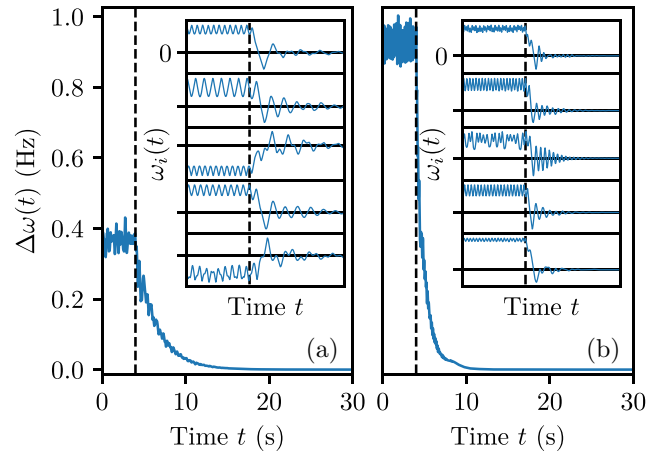


FIG. 8. Time-delayed feedback control: Standard deviation of frequencies $\Delta\omega(t)$ versus time t . The insets show the frequencies $\omega_i(t)$ versus time t of five arbitrary solitary nodes. Panel (a) corresponds to the distribution P^G with $P^{\text{Max}} \approx 817$ MW and (b) to P^R with $P^{\text{Max}} \approx 729$ MW. The dashed vertical lines indicate the onset of control; delay time $\tau = 4$ s. The feedback gain g_i is set to $g_i = 1$ for solitary nodes and $g_i = 0$ for other nodes; other parameters as in Fig. 5(d) for panel (a) and Fig. 6(d) for panel (b).

$\Delta\omega(t)$ exponentially decays ($\propto e^{-t/t_c}$) as soon as the control is activated and reaches $\Delta\omega(t) = 0$ with a characteristic time $t_c \approx 2.58$ s ($t_c \approx 0.92$ s). When the control is turned off at $t = 40$ s, the synchronized states persist and are Lyapunov stable ($\lambda_1 = 0$). In other words by applying the proposed control method on few solitary nodes out of a big network, we have the possibility to synchronize and stabilize the network. The control is not necessarily active all the time, since it can be switched on when solitary nodes emerge and it turns off automatically when the node is synchronized again, i.e., $\omega_i(t) = 0$.

In the following we propose to apply the control term only to a small subset of nodes selected according to their dynamical properties. In particular we aim at designing a control strategy based on the dynamical properties of the system that allows us to attain synchronization by controlling few nodes only (i.e., fewer nodes than the ensemble of solitary nodes shown in Fig. 8), thus speeding up the efficiency of control. In order to find such a set, different control strategies are proposed in the following: (i) The first strategy takes into consideration all solitary nodes, sorted in descending order of ξ_i ; (ii) the second strategy orders the solitary nodes by their absolute average frequency $|\langle \omega_i \rangle_t|$; and (iii) the third strategy consider all nodes, not only solitary ones, randomly picked. The outcome of the different strategies is shown in Figs. 9(a)–9(c) and 9(d)–9(f) for the bimodal Gaussian distribution P^G and the real-world distribution P^R , respectively. First, strategy (i) is able to achieve stability if just one node is controlled and frequency synchronization if the number of controlled solitary nodes is sufficiently large: eight controlled nodes for both P^G and P^R . Strategy (ii) requires four controlled nodes for stabilization and eight for synchronization in the case of P^G and one controlled node for stabilization and nine nodes for synchronization in case of P^R . The third strategy is not able to frequency-synchronize and stabilize; it can at most mitigate

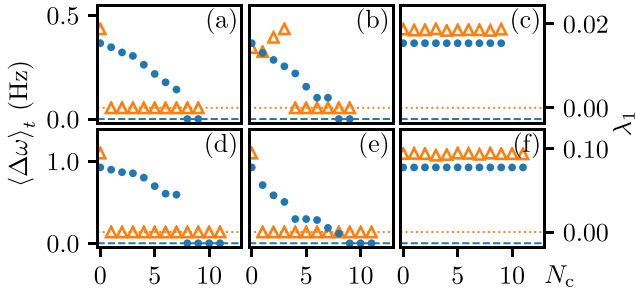


FIG. 9. Efficiency of time-delayed feedback control: Time-averaged frequency deviation $\langle \Delta\omega \rangle_t$ (blue dots) and maximum Lyapunov exponent λ_1 (orange triangles) vs number of controlled nodes N_c following different control strategies: [(a) and (d)] Solitary nodes sorted in descending order of ξ_i . [(b) and (e)] Solitary nodes sorted in descending order of $|\omega_i|$. [(c) and (f)] Randomly picked nodes. At each step of each control strategy, one more node is controlled, picked from one of the three mentioned lists, and both the level of synchronization and the instability are recalculated via $\langle \Delta\omega \rangle_t$ and λ_1 . Panels (a)–(c) correspond to the distribution P^G and (d)–(f) to P^R . The dashed line marks $\langle \Delta\omega \rangle_t = 0$, the dotted line denotes $\lambda_1 = 0$. Control acts for a duration of 40 s and is then turned off; delay time $\tau = 4$ s, feedback gain $g = 1$, time averages over 80 s, and operating points $K \approx 817$ ($K \approx 729$) for P^G (P^R). Other parameters as in Fig. 5(d) for (a)–(c) and Fig. 6(d) for (d)–(f).

to some extent the desynchronization and the instability. For the given setup, strategy (i) is the best choice: It is particularly efficient since the Lyapunov vector is recalculated every time when an additional solitary node is controlled, thus taking into account the interplay between solitary states and emerging instabilities. However, both strategies (i) and (ii) highlight the role played by solitary nodes, a role that will be clarified in more detail in the next section.

C. Lyapunov analysis

The presence of solitary nodes deeply influences the dynamics emerging in the system, since they behave almost independently, adding complexity and conveying the instability. In particular the role played by the solitary nodes can be understood by the change in the Lyapunov spectrum when the control strategy (i) is applied, i.e., when solitary nodes are controlled, ordered according to their Lyapunov vector component (for the definition of the other strategies see previous section).

If we first consider the bimodal Gaussian natural frequency distribution, the uncontrolled state is characterized by a cluster of synchronized oscillators plus nine solitary nodes. The system is chaotic and the maximum Lyapunov exponent is positive [see Fig. 10(a)]: The interplay between solitary nodes and cluster state gives rise to low-dimensional chaos in the system. When the first solitary node is controlled [Fig. 10(b)], the dynamics becomes quasiperiodic and the collective behavior is a high-dimensional torus, as can be deduced by the consistent number of eight Lyapunov exponents that are exactly zero. Each solitary node, at the microscopic level, moves with an average velocity which is different from the velocity of the cluster and from the velocity of the other solitary states: The self-emergent dynamics, at the macroscopic

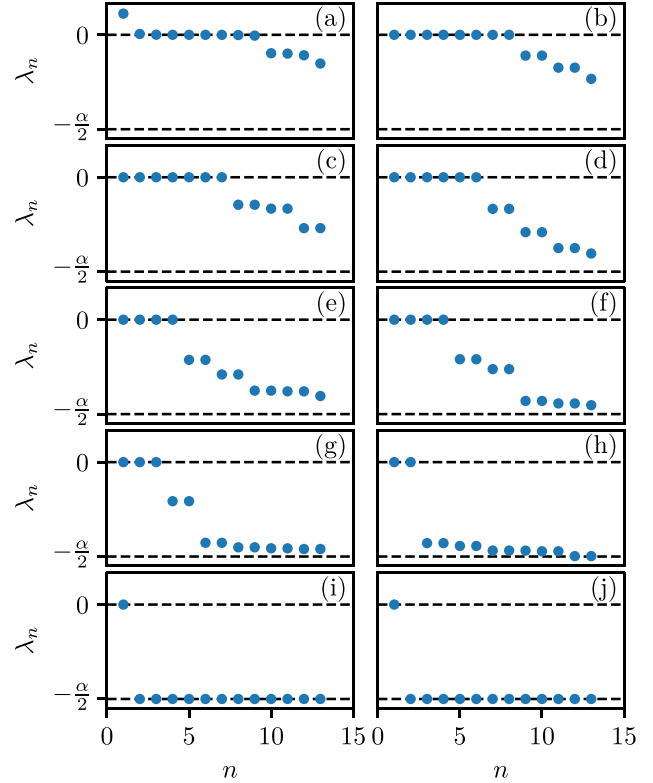


FIG. 10. Bimodal Gaussian natural frequency distribution, control strategy (i): Lyapunov exponents λ_n versus n for $K = 817$ MW. For simplicity only the first 13 exponents of the spectrum are plotted. Panels (a) to (j) are arranged according to the number of controlled nodes N_c increasing by one from $N_c = 0$ to $N_c = 9$. Lyapunov exponents are expressed in units of $\Delta t^{-1} = 5$ s $^{-1}$.

level, is a quasiperiodic motion characterized by multiple incommensurable frequencies. When solitary nodes are controlled and frequency synchronized to the cluster, they do no longer contribute to the collective dynamics with their own frequency, thus decreasing the dimensionality of the macroscopic behavior. Thus, the further control of more solitary nodes has the effect of stabilizing the system: Negative exponents becomes more and more negative while the zero ones become negative. When five solitary states are controlled, the macroscopic dynamics evolves on a two-dimensional torus [see Fig. 10(f)]. This can be explained considering that in the system under investigation one might expect two Lyapunov exponents to be zero due to the symmetries of the system: One is always present for a system with continuous time, while the second zero exponent is related to the invariance of the model under uniform phase shift. Therefore when five solitary nodes are controlled, two exponents are zero due to symmetries, while the other two zero exponents identify the emergent quasiperiodicity. Finally, when the system is synchronized, thanks to the control of eight solitary nodes, the typical spectrum of a stable periodic synchronized state appears, with a negative plateau at $\lambda_n = -\alpha/2$ (for $1 < n < 2N - 1$) and $\lambda_1 = 0$ [see Figs. 10(i) and 10(j)]. The synchronized state is degenerate and the phase shift of all the phases corresponds to a perturbation along the orbit of the fully synchronized state, which explains why the two invariances, and thus the

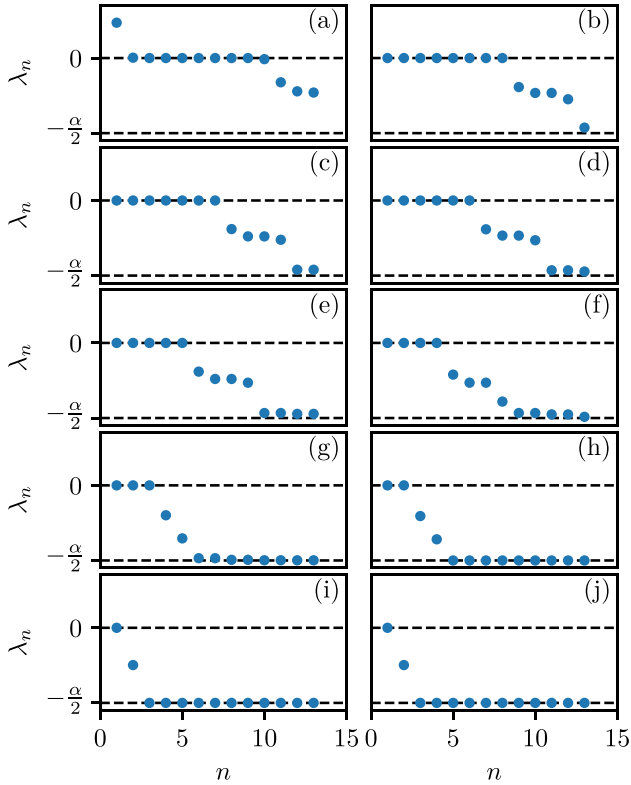


FIG. 11. Real-world natural frequency distribution, control strategy (i): Lyapunov exponents λ_n versus n for $K = 729$ MW. For simplicity only the first 13 exponents of the spectrum are plotted. Panels (a) to (j) are arranged according to the number of controlled nodes N_c increasing by one from $N_c = 0$ to $N_c = 11$. Lyapunov exponents are expressed in units of $\Delta t^{-1} = 5 \text{ s}^{-1}$.

Lyapunov exponents, coincide, as already shown in Ref. [51] for a globally coupled network.

A similar behavior can be observed for the real-world natural frequency distribution case, where the initial uncontrolled state is chaotic ($\lambda_1 > 0$) and 11 solitary nodes emerge from the synchronized cluster state [see Fig. 11(a)]. When the solitary state with largest Lyapunov component is controlled and synchronized to the cluster, the system is no longer unstable, which indicates that the instability was conveyed by the selected solitary node [see Fig. 11(b)]. Due to the interaction of the remaining solitary states, characterized by different average frequencies, the collective dynamics of the system turns out to be quasiperiodic and high dimensional. The dimensionality of the quasiperiodic motion is reduced by controlling more and more nodes and results in a two-dimensional torus when five solitary nodes are controlled [see Fig. 11(f)]. Finally, the system is synchronized when eight solitary states are controlled [see Fig. 11(i)], while the additional control of further nodes does not alter nor enhance the synchronization.

D. Topological features vs extreme events

In Ref. [30] numerical evidence was given that dead ends and dead trees undermine basin stability of nodes in Kuramoto power grid networks, which means that the basin of attraction of the frequency synchronized solution for single nodes tends

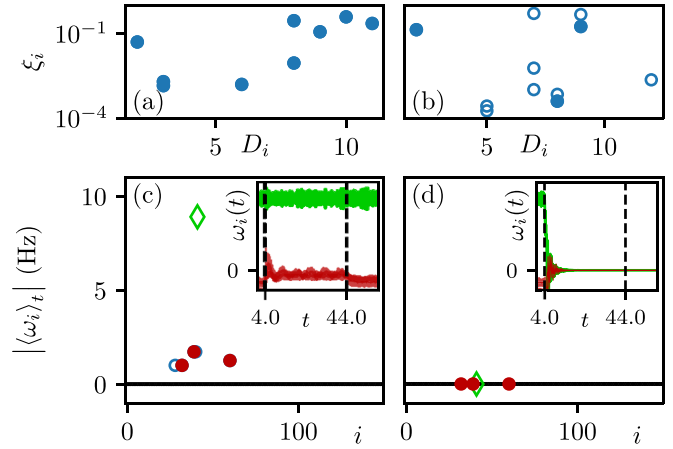


FIG. 12. Source of solitary nodes: Lyapunov vector components ξ_i versus maximum neighborhood degree D_i for (a) P^G and (b) P^R . Only solitary nodes are shown, and filled circles identify nodes which belong to dead trees. [(c) and (d)] Absolute time-averaged frequency $|\langle \omega_i \rangle_t|$ versus node index i for P^G , where $4\Delta P$ is added to the inherent frequency of an arbitrary nonsolitary node k (green diamond). In (c) dead-tree nodes (filled circles) adjacent to k are controlled and in (d) k is controlled. The black line indicates the synchronized cluster. The instantaneous frequencies $\omega_i(t)$ of node k (light green) and dead-tree nodes adjacent to k (dark red) versus time are shown in the insets. Vertical dashed lines mark activation and deactivation of control. Parameters as in Figs. 4 and 7, time averages over 80 s.

to be small if a node is placed at a dead end, thus making such nodes hard to synchronize. The general pattern of these most peripheral nodes looks very similar to the pattern of most sensitive nodes numerically found in Ref. [52] and partially explained on the basis of resistance distance centralities in Ref. [53].

Indeed, in the case of the bimodal Gaussian distribution P^G , all the identified solitary nodes belong to a dead tree [see Fig. 12(a)]. However, this trend cannot be observed for the real-world distribution P^R , where just 3 of the 11 solitary nodes belong to a dead tree [see Fig. 12(b)] and dead trees do not correspond to the most unstable nodes. In general we have observed that the most unstable solitary nodes, for P^G , are dead ends adjacent to well connected nodes, whereas for P^R they are nodes with $P_i > 4\Delta P$, where ΔP is the standard deviation of the distribution. The discrepancy between the two cases can be explained if, starting from P^G , we arbitrarily add $4\Delta P$ to the net power ($\hat{=}$ inherent frequency) of a nonsolitary node k . This altered node then becomes solitary and causes other adjacent nodes to become solitary, some of them belonging to dead trees. If we control all the newly emerged solitary dead trees, then the system does not synchronize and the dynamics of node k is almost unchanged [Fig. 12(c)], whereas we can achieve synchronization via controlling node k only [Fig. 12(d)]. This means that dead trees are fundamental in determining the power grid stability whenever the power distribution does not contain fat tails or *extreme events*, which is the case for P^G ; for the real-world distribution P^R , however, nodes with significant power difference are common and the stability is undermined by these nodes rather than by dead trees.

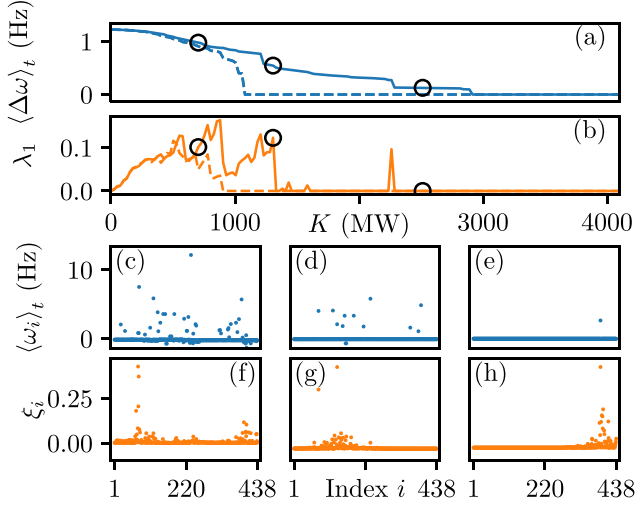


FIG. 13. German power grid with real-world distribution P^R using the extended model: (a) Average frequency deviation $\langle \Delta\omega \rangle_t$ and (b) largest Lyapunov exponent λ_1 versus coupling strength K . The solid lines (dashed lines) correspond to the adiabatic upswep (downsweep) of K . [(c)–(e)] Average frequencies $\langle \omega_i \rangle_t$ and [(f)–(h)] Lyapunov vector components ξ_i versus node index i for the K values marked by black circles in the top panels from left to right. Parameters: $m_v = 1$, $E_{f,i} = 1$, $X_i = 1$. Lyapunov exponents and vectors calculated for a duration of 8×10^3 s. Lyapunov exponents are expressed in units of $\Delta t^{-1} = 5 \text{ s}^{-1}$. Other parameters as in Fig. 6.

IV. RESULTS FOR A LOSSLESS NETWORK OF SYNCHRONOUS MACHINES

Applying the same procedure as previously done for the standard Kuramoto model with inertia with different natural frequency distributions, we perform an adiabatic parameter scan in K , thus identifying the synchronization transition of the system during the upswep and downsweep protocols. The system is initialized at $K = 0$ with uniformly distributed initial conditions not only for phases and frequencies $\{\theta_i, \dot{\theta}_i\}$ but also for the voltage amplitudes $\{E_i\}$, that are set uniformly random: $E_i(0) \in [0.5, 1.5)$.

As for the previously investigated setups, the system undergoes a hysteretic transition to synchronization [see Fig. 13(a)]. It shows an asynchronous state for low coupling values K and partially synchronized states for intermediate K values [Figs. 13(d) and 13(e)]. In particular the number of whirling nodes diminishes with increasing K and it is possible to identify a state, in proximity of the synchronization transition, where almost all nodes are synchronized, while few of them are solitary nodes still oscillating with average frequency different from zero [Fig. 13(e)]. Similarly to the previous setups, the Lyapunov vector is (mostly) localized around solitary nodes [see Figs. 13(c)–13(h) corresponding to different stages of the adiabatic upswep], thus indicating that solitary nodes are leading the synchronization transition even when considering voltage dynamics. Finally, the system is chaotic for a larger K interval [Fig. 13(b)] as compared to the original Kuramoto model with inertia.

Strategies (i) and (ii) to synchronize and stabilize the system are applied to the partially synchronized state at $K \approx$

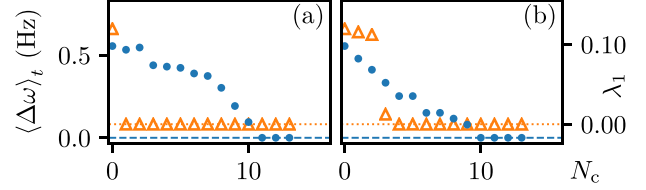


FIG. 14. Efficiency of time-delayed feedback control for the German power grid with real-world distribution P^R using the extended model: Time-averaged frequency deviation $\langle \Delta\omega \rangle_t$ (blue dots) and maximum Lyapunov exponent λ_1 (orange triangles) vs number of controlled nodes N_c following different control strategies: (a) Solitary nodes sorted in descending order of ξ_i ; (b) solitary nodes sorted in descending order of $|\langle \omega_i \rangle_t|$. The dashed line marks $\langle \Delta\omega \rangle_t = 0$ and the dotted line denotes $\lambda_1 = 0$. Control acts for a duration of 40 s and is then turned off; delay time $\tau = 4$ s and feedback gain $g = 1.3$, $K \approx 1307$ MW [middle point of Fig. 13(a)]. Other parameters as in Fig. 13.

1307 MW [see Fig. 13(d) and 13(g)], where 13 solitary nodes are present: A comparison of the strategies is shown in Fig. 14.

The first strategy requires control of one node in order to stabilize the system and 11 to synchronize, whereas the second strategy performs worse when stabilizing the system (4 nodes required) but performs better when synchronizing (10 nodes). However both control schemes require not all solitary nodes to be controlled in order to achieve synchronization and stability. All in all our approach is not only applicable to the example systems presented in Sec. III but works for different models. In Appendix B, the generality of the approach will be further explained considering different topologies and different operating points. Even though it is not possible to provide an analytical proof of the efficiency and generality of our control approach, our results indicate how powerful and robust time-delayed feedback control is and that it can be applied to a diversity of topologies and power grid models. The hysteretic nature of the transition to synchronization, the bistability of the system, and the emergence of solitary states driving the dynamics are fundamental ingredients for enhancing the stability of power grids, which, as far as we know, have not been recognized until now.

V. CONCLUSIONS

In conclusion, we have proposed a time-delayed feedback control scheme to restore frequency synchronization and stability of the power grid after perturbations. To this purpose we have first studied the Kuramoto model with inertia in the presence of two different bimodal distributions of generator and load power (an artificial distribution, and one adapted from the real German high-voltage transmission grid), which both lead to a fully frequency synchronized, stable network for large transmission capacities K . We have focused on the operating regime of intermediate K characterized by a number of solitary nodes whose mean frequency deviates from that of all other nodes.

We have shown that stability and synchronization can be enhanced by time-delayed feedback control in this K regime by applying delayed feedback to a small subset of nodes: Frequency synchronization and stability can be restored in a

short time and persist even if control is turned off. Different control strategies were tested. For the shown setup the best strategy is to control the most unstable solitary nodes, characterized by the largest Lyapunov vector components. However, both strategies (i) and (ii) are efficient, being based on the solitary nodes that turn out to be fundamental in regulating the dynamics of the system. Solitary nodes exhibit independent dynamics, giving rise to low-dimensional chaos that turns into high-dimensional quasiperiodic motion when the most unstable node is controlled, until synchronization is achieved. Therefore, due to their independence, the set of controlled nodes cannot be much smaller than the number of solitary nodes.

The proposed fast-acting control method might offer an interesting approach to cure disturbances in real-world power grids, due to its general applicability and validity, as shown in Sec. IV, where we have applied our control strategy to a more sophisticated model including the voltage dynamics [35] and, more in general, as shown in Appendix B, where we have extended our analysis to a different network (i.e., the Italian grid) and to different operating points keeping the German grid topology.

Finally, the main message of the paper does not rely on the specific control method in use but rather on the designed control strategy based on the dynamical properties of the system (i.e., the emergence of solitary states), which allows us to attain synchronization by controlling few nodes, thus speeding up the efficiency of control. To sustain this affirmation we have compared the efficiency of delayed feedback control and feedback control proportional to the instantaneous frequency, thus showing that both control methods are able to synchronize the grid with our strategy. Time-delayed feedback control remains preferable since it is effective even at smaller gain couplings, as shown in Appendix A.

ACKNOWLEDGMENTS

We acknowledge A. Torcini and S. Lepri for valuable discussions. Funded by the Deutsche Forschungsgemeinschaft (DFG, German Research Foundation), Projektnummer 163436311-SFB 910.

APPENDIX A: PARAMETER CHOICE

1. Kuramoto model with inertia

As already detailed in Sec. II A, the Kuramoto model with inertia describes the phase and frequency dynamics of N coupled synchronous machines, i.e., generators or consumers within the power grid, where mechanical and electrical phase and frequency are assumed to be identical. The N dynamic equations describing the time evolution of the phase $\theta_i(t)$ and frequency $\dot{\theta}_i(t) = \frac{d\theta_i}{dt}$ of node $i = 1, \dots, N$ are given by Eq. (1). In particular α represents the dissipation parameter and takes typical values of $0.1\text{--}1 \text{ s}^{-1}$ [30,36]. However, in a realistic power grid there are additional sources of dissipation, especially Ohmic losses, and losses caused by damper windings [36], which are not taken into account directly in the coupled oscillator model. Therefore, for this parameter we have chosen slightly higher values: $\alpha = 5/6 \text{ s}^{-1}$ when a bimodal Gaussian distribution is considered and $\alpha = 2 \text{ s}^{-1}$ when the

real-world distribution is taken into account to describe the distribution of the net power P_i . Different dissipation values are necessary for the different distributions in order to obtain comparable setups, i.e., unstable, partially synchronized states at comparable coupling strengths, $K = 817 \text{ MW}$ for the bimodal Gaussian distribution and $K = 729 \text{ MW}$ for the real-world one.

For both net power distributions, the coupling strength K , which represents the maximum power transmission capacity of transmission lines, was set homogeneously throughout the grid. A more realistic approach would have been to use a coupling matrix K_{ij} , containing not only the topology but also individual transmission capacities to schematize different transmission line lengths. However, the goal of the present paper is to gain insight into the principal behavior of large power grids depending on the network topology and their capability to synchronize by controlling a minimal set of nodes and, for a proof of principle of our control approach, the choice of identical transmission lines suffices. The choice of using simplified homogeneous transmission line capacities (coupling constants) turned out to be a good compromise when using heterogeneous power distributions, whose realistic values were available in the open data source as opposed to the transmission line data.

Equation (1) can be simplified by rescaling the parameters $m := \frac{1}{\alpha}$, $\Omega_i := \frac{P_i}{I_i \omega_G \alpha}$, $\kappa := \frac{K}{I_i \omega_G \alpha}$, thus giving

$$m\ddot{\theta}_i + \dot{\theta}_i = \Omega_i + \kappa \sum_{j=1}^N A_{ij} \sin(\theta_j - \theta_i). \quad (\text{A1})$$

In comparison with Eq. (1), the inertial mass m now represents the inverse of the dissipation α in the grid, and the coupling constant κ now represents the maximum power which can be transmitted between two connected nodes. Moreover, each node i , when uncoupled, oscillates with an angular frequency Ω_i , referred to as *natural frequency* or *inherent frequency*. Therefore the distribution of natural frequencies and the distribution of net power P_i are equivalent, up to a constant factor.

Finally, adiabatic simulations (upsweep of κ) are performed to measure the level of synchronization in the network starting from the asynchronous state toward the partially synchronized state. In particular the rescaled coupling strength κ is increased from $\kappa = 0$ to $\kappa = 60$ in steps of $\Delta\kappa = 0.4$ (from $\kappa = 0$ to $\kappa = 60$ in steps of $\Delta\kappa = 0.2$) for the bimodal Gaussian distribution (real-world distribution, respectively). Specifically, for the bimodal Gaussian distribution with $\alpha = 5/6 \text{ s}^{-1}$, $I_i = 40 \times 10^3 \text{ kg m}^2$, $\omega_G = 2\pi 50 \text{ Hz}$, and $\Delta\kappa = 0.4/\Delta t$ one obtains $\Delta K = \Delta\kappa I_i \omega_G \alpha \approx 21 \text{ MW}$ if a time unit $\Delta t = 0.2 \text{ s}$ is considered.

2. Time-delayed feedback control

The main message of the manuscript is the importance of the designed control strategy, based on the investigation of the dynamical properties of the system, to enhance power grid synchronization and stability. In particular the designed strategy allows us to affirm that some nodes are more important than the others and we can attain synchrony by controlling only those. Then we have used time-delayed feedback because it is a common control method in nonlinear dynamics but

TABLE I. Control performance using the German grid with P^R : Each cell shows the number of remaining solitary nodes after control, using instantaneous feedback and delayed feedback with different delays τ and feedback gains g . The nodewise gain g_i is set to $g_i = g$ for solitary nodes and $g_i = 0$ for other nodes. Without control the system contains 11 solitary nodes. Control acts for a duration of 40 s and is then turned off; other parameters as in Fig. 6(d).

$\tau \downarrow$	$g \rightarrow$	0.25	0.50	1.00	1.50	2.00	3.00
Instantaneous		7	4	1	1	0	0
1 s		8	4	0	0	0	0
2 s		8	4	0	0	0	0
4 s		5	3	0	0	0	0
6 s		5	1	0	0	0	0
8 s		5	1	0	0	0	0

quite new in the context of power grids; however, any other reasonable control term could have been used equivalently. In the following we report a comparison between delayed feedback control versus instantaneous feedback control to prove the importance of the obtained findings as a general result in the nonlinear dynamics framework. The dynamics of the Kuramoto model with inertia in presence of instantaneous feedback control reads

$$\ddot{\theta}_i + \alpha \dot{\theta}_i = \frac{P_i}{I\omega_G} + \frac{K}{I\omega_G} \sum_{j=1}^N A_{ij} \sin(\theta_j - \theta_i) - g_i \alpha \dot{\theta}_i. \quad (\text{A2})$$

The comparison shows that both in the Kuramoto model with inertia (see Table I) as well as in the extended model (see Table II) a larger feedback gain is required for instantaneous feedback in order to synchronize all solitary nodes. Delayed feedback allows the control term to lag behind with respect to the instantaneous frequency, thus sustaining larger levels of control input after control activation. However, the control strategy works even with a different control method and synchronization can be always attained. Without loss of generality we have chosen in the main text $\tau = 4$ s and $g = 1$, if not stated differently.

TABLE II. Control performance using the extended model and the German grid with P^R : Each cell shows the number of remaining solitary nodes after control, using instantaneous feedback and delayed feedback with different delays τ and feedback gains g . The nodewise gain g_i is set to $g_i = g$ for solitary nodes and $g_i = 0$ for other nodes. Without control the system contains 13 solitary nodes. Control acts for a duration of 40 s and is then turned off; other parameters as in Fig. 13(d).

$\tau \downarrow$	$g \rightarrow$	0.25	0.50	1.00	1.50	2.00	3.00
Instantaneous		9	7	5	2	2	0
1 s		9	7	5	1	0	0
2 s		9	6	1	0	0	0
4 s		9	6	1	0	0	0
6 s		9	6	1	0	0	0
8 s		9	5	1	0	0	0

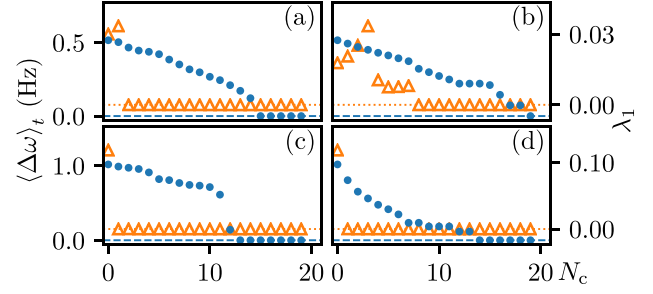


FIG. 15. Efficiency of time-delayed feedback control for a different operating point: Time-averaged frequency deviation $\langle \Delta\omega \rangle_t$ (blue dots) and maximum Lyapunov exponent λ_1 (orange triangles) vs number of controlled nodes N_c following different control strategies: [(a) and (c)] Solitary nodes sorted in descending order of ξ_i ; [(b) and (d)] solitary nodes sorted in descending order of $|\omega_i|$. Panels (a) and (b) correspond to the distribution P^G and (c) and (d) to P^R . The dashed line marks $\langle \Delta\omega \rangle_t = 0$ and the dotted line denotes $\lambda_1 = 0$. Control acts for a duration of 40 s and is then turned off; delay time $\tau = 4$ s and feedback gain $g = 1.5$ ($g = 1$) for P^G (P^R). Other parameters as in Fig. 5 for the top panels (Fig. 6 for the bottom panels). In comparison to Fig. 9, the coupling strengths K are smaller ($K \approx 565$ MW and $K \approx 578$ MW for P^G and P^R , respectively) and the initial sets of solitary nodes are bigger, thus being more difficult to control.

APPENDIX B: GENERALITY OF THE RESULTS

In order to show that the efficiency of our proposed control strategies is not restricted to the setups shown in the main text, we will present additional results: (a) keeping the setups shown in the main text but analyzing different operating points and different configurations by considering different coupling strengths and (b) taking into consideration a different topology.

1. Different operating points

In this section we present the results for a different operating point, thus giving rise to a different configuration of solitary nodes. In particular, keeping the same setups presented in the main text, we show a comparison between the strategies (i) and (ii) obtained when the system is evaluated at different coupling strengths, thus investigating different working points with respect to the results shown in the main text. For the bimodal Gaussian distribution P^G , we investigate the state at $K \approx 565$ MW, which is a partially synchronized state found during the upsweep protocol, characterized by 19 solitary nodes. This configuration is unstable, with $\lambda_1 = 0.0144 \pm 0.0005$. Regarding the real-world distribution P^R , the different working point that we have investigated is characterized by $K \approx 578$ MW, 19 solitary nodes, and $\lambda_1 = 0.116 \pm 0.005$.

The outcome of the control schemes is shown in Fig. 15. For the P^G distribution strategy (i) requires the control of 2 solitary nodes to stabilize the system and 15 to synchronize, while strategy (ii) requires the control of 8 nodes to stabilize and 19 to synchronize the system. For the real-world distribution both strategies require one controlled node to stabilize. Synchronization is reached with 13 and 14 nodes using strategy (i) and (ii), respectively.

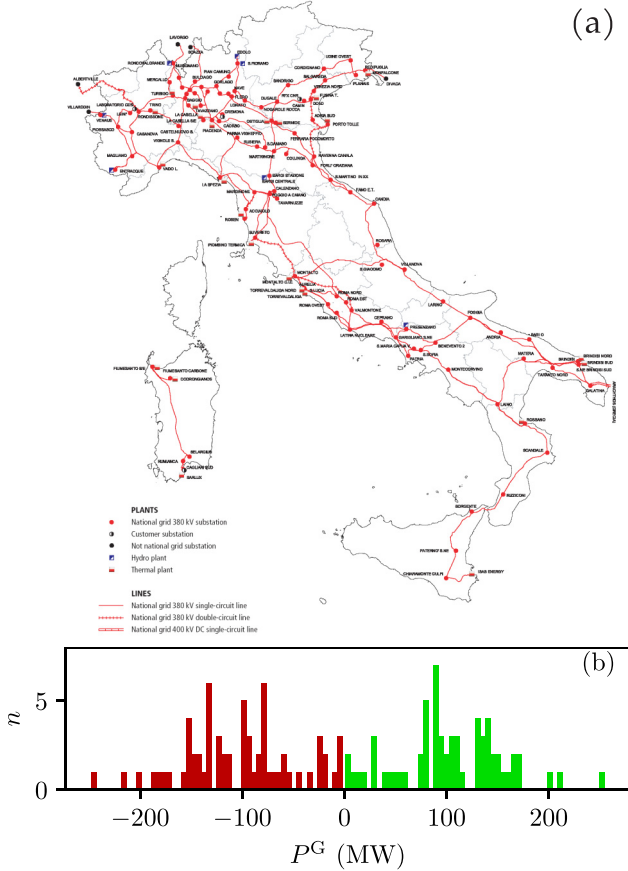


FIG. 16. (a) Map of the Italian ultra-high-voltage power grid, consisting of 127 nodes connected by 171 transmission lines (red lines) [54]. (b) Histogram shows a realization of an artificial bimodal Gaussian distribution of net power with $N = 127$, $P_0 = 105$ MW, $\sigma = P_0/2$. The light green (dark red) bars correspond to generators (consumers).

2. Italian grid

In this section we apply our control strategy to a different grid topology. The dynamics of the single node is still described by Eq. (1), but we now consider the Italian high-voltage (380 kV) power grid (Sardinia excluded), which is composed of $N = 127$ nodes, divided into 34 generators (hydroelectric and thermal power plants) and 93 consumers, connected by 171 transmission lines [54]. This network is characterized by a quite low average connectivity $\langle N_c \rangle = 2.865$, due to the geographical distributions of the nodes along Italy [see Fig. 16(a)]. Since we have no access to a distribution of generator powers and nodal power consumption, we restrict the application of our method to the artificial distribution, using a bimodal Gaussian distribution [shown in Fig. 16(b)] with the same probability density function as the one used for the German grid [see Eq. (4) of the main text].

Like for the German grid, the synchronization transition is hysteretic [see Fig. 17(a)], but the formation of frequency clusters at different stages of the upswEEP protocol is more pronounced since the local architecture favours a splitting based on the proximity of the oscillators. At $K \approx 461$ MW [middle black point of Fig. 17(a)] the system is partially

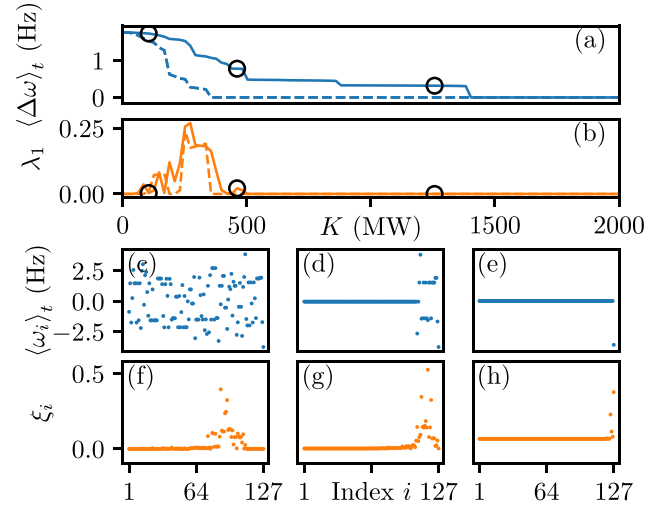


FIG. 17. Italian power grid with Gaussian distribution P^G : (a) Average frequency deviation $\langle \Delta\omega \rangle_t$ and (b) largest Lyapunov exponent λ_1 versus coupling strength K . The solid lines (dashed lines) correspond to the adiabatic upswEEP (downswEEP) of K . [(c)–(e)] Average frequencies $\langle \omega_i \rangle_t$ and [(f)–(h)] Lyapunov vector components ξ_i versus node index i for K values marked by the black circles in the top panels from left to right. Lyapunov exponents and vectors calculated for a duration of 2×10^4 . Other parameters as in Fig. 5.

synchronized and unstable ($\lambda_1 > 0$): It represents a big cluster of locked oscillators with zero average frequency and 20 unsynchronized whirling oscillators [see Fig. 17(d)]. Besides the main frequency-synchronized cluster, two other clusters can be found: one with positive and one with negative average frequency, consisting of eight and five nodes, respectively. The remaining seven nodes are solitary. As before, we will take this state as an example to be controlled using our proposed strategies. For smaller coupling the system is unstable, but completely asynchronous [see Figs. 17(b) and 17(c)], while for larger coupling the system is (almost) completely synchronized [see Fig. 17(e)]: One solitary state corresponding to the last node in Sicily hardly synchronizes due to the peripheric position in the network.

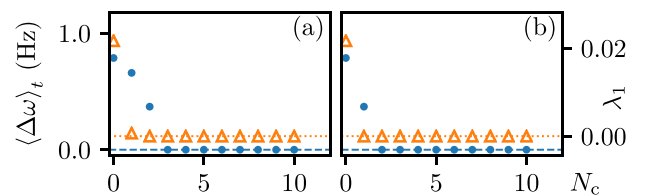


FIG. 18. Efficiency of time-delayed feedback control for the Italian grid: Time-averaged frequency deviation $\langle \Delta\omega \rangle_t$ (blue dots) and maximum Lyapunov exponent λ_1 (orange triangles) vs number of controlled nodes N_c following different control strategies. (a) Solitary nodes sorted in descending order of ξ_i . (b) Solitary nodes sorted in descending order of $|\langle \omega_i \rangle_t|$. The dashed lines mark $\langle \Delta\omega \rangle_t = 0$ and the dotted lines denote $\lambda_1 = 0$. Control acts for a duration of 40 s and is then turned off; delay time $\tau = 4$ s and feedback gain $g = 1$, $K \approx 461$ MW (middle point of Fig. 17). Other parameters as in Fig. 17.

In Fig. 18 a comparison of strategies (i) and (ii) is presented. First, as for the German grid, the delayed feedback control is able to synchronize and stabilize the grid when enough nodes are controlled. Strategy (i), which controls preferably the most unstable nodes, sorted according to their Lyapunov vector component ξ_i , needs two nodes to stabilize and three controlled nodes to synchronize the system [Fig. 18(a)]. On the other hand, by employing strategy (ii),

which orders the controlled nodes with respect to their frequency deviation $|\langle \omega_i \rangle_t|$, the control of one node is required to stabilize and two controlled nodes to synchronize the system [Fig. 18(b)]. In both cases a remarkably small fraction of the 20 whirling nodes has to be controlled to gain the suitable conditions for operating power grids, thus highlighting the role played by solitary nodes in driving the network dynamics.

-
- [1] A. Pikovsky, M. G. Rosenblum, and J. Kurths, *Synchronization: A Universal Concept in Nonlinear Sciences* (Cambridge University Press, Cambridge, 2001).
- [2] S. Boccaletti, A. N. Pisarchik, C. I. del Genio, and A. Amann, *Synchronization: From Coupled Systems to Complex Networks* (Cambridge University Press, Cambridge, 2018).
- [3] C. van Vreeswijk, *Phys. Rev. E* **54**, 5522 (1996).
- [4] C. van Vreeswijk, *Phys. Rev. Lett.* **84**, 5110 (2000).
- [5] S. H. Strogatz, *Nature* **410**, 268 (2001).
- [6] Y. Maistrenko, B. Penkovsky, and M. Rosenblum, *Phys. Rev. E* **89**, 060901(R) (2014).
- [7] P. Jaros, S. Brezetsky, R. Levchenko, D. Dudkowski, T. Kapitaniak, and Y. Maistrenko, *Chaos* **28**, 011103 (2018).
- [8] P. Milan, M. Wächter, and J. Peinke, *Phys. Rev. Lett.* **110**, 138701 (2013).
- [9] D. Heide, L. von Bremen, M. Greiner, C. Hoffmann, M. Speckmann, and S. Bofinger, *Renew. Energy* **35**, 2483 (2010).
- [10] D. Heide, M. Greiner, L. von Bremen, and C. Hoffmann, *Renew. Energy* **36**, 2515 (2011).
- [11] T. Coletta, R. Delabays, I. Adagideli, and P. Jacquod, *New J. Phys.* **18**, 103042 (2016).
- [12] Union for the Co-ordination of Transmission of Electricity (UCTE), Final Report - System Disturbance on 4 November 2006, UCTE, Brussels, 2007.
- [13] Central Electricity Regulatory Commission (CERC), Report on the grid disturbance on 30th July 2012 and grid disturbance on 31st July 2012, CERC, New Delhi, 2012.
- [14] A. E. Motter and Y. C. Lai, *Phys. Rev. E* **66**, 065102(R) (2002).
- [15] S. V. Buldyrev, R. Parshani, G. Paul, H. Eugene Stanley, and H. Shlomo, *Nature* **464**, 1025 (2010).
- [16] J. W. Bialek, in *2007 IEEE Lausanne Power Tech* (IEEE, New York, 2007), pp. 51–56.
- [17] B. Schäfer, D. Witthaut, M. Timme, and V. Latora, *Nat. Commun.* **9**, 1975 (2018).
- [18] B. Schäfer, C. Beck, K. Aihara, D. Witthaut, and M. Timme, *Nat. Energy* **3**, 119 (2018).
- [19] I. Simonsen, L. Buzna, K. Peters, S. Bornholdt, and D. Helbing, *Phys. Rev. Lett.* **100**, 218701 (2008).
- [20] H. D. Chiang, *Direct Methods for Stability Analysis of Electric Power Systems: Theoretical Foundation, BCU Methodologies, and Applications* (John Wiley & Sons, New York, 2010).
- [21] M. Anvari, G. Lohmann, M. Waechter, P. Milan, E. Lorenz, D. Heinemann, M. Reza Rahimi Tabar, and J. Peinke, *New J. Phys.* **18**, 063027 (2016).
- [22] M. Tyloo, R. Delabays, P. Jacquod, *Phys. Rev. E* **99**, 062213 (2019).
- [23] B. Schäfer, M. Matthiae, M. Timme, and D. Witthaut, *New J. Phys.* **17**, 015002 (2015).
- [24] P. J. Menck, J. Heitzig, N. Marwan, and J. Kurths, *Nat. Phys.* **9**, 89 (2013).
- [25] M. Rohden, A. Sorge, M. Timme, and D. Witthaut, *Phys. Rev. Lett.* **109**, 064101 (2012).
- [26] D. Witthaut and M. Timme, *New J. Phys.* **14**, 083036 (2012).
- [27] E. B. T. Tchuisseu, D. Gomila, P. Colet, D. Witthaut, M. Timme, and B. Schäfer, *New J. Phys.* **20**, 083005 (2018).
- [28] A. E. Motter, S. A. Myers, M. Anghel, and T. Nishikawa, *Nat. Phys.* **9**, 191 (2013).
- [29] F. Dörfler, M. Chertkov, and F. Bullo, *Proc. Natl. Acad. Sci. USA* **110**, 2005 (2013).
- [30] P. J. Menck, J. Heitzig, J. Kurths, and H. J. Schellnhuber, *Nat. Commun.* **5**, 3969 (2014).
- [31] D. Witthaut, M. Rohden, X. Zhang, S. Hallerberg, and M. Timme, *Phys. Rev. Lett.* **116**, 138701 (2016).
- [32] K. Pyragas, *Phys. Lett. A* **170**, 421 (1992).
- [33] E. Schöll and H. G. Schuster (Eds.), *Handbook of Chaos Control* (Wiley-VCH, Weinheim, 2008).
- [34] G. Filatella, A. H. Nielsen, and N. F. Pedersen, *Eur. Phys. J. B* **61**, 485 (2008).
- [35] K. Schmietendorf, J. Peinke, R. Friedrich, and O. Kamps, *Eur. Phys. J. Spec. Top.* **223**, 2577 (2014).
- [36] J. Machowski, J. Bialek, and J. R. Bumby, *Power System Dynamics: Stability and Control*, 2nd ed. (John Wiley & Sons, New York, 2008).
- [37] S. H. Horowitz and A. G. Phadke, *Power System Relaying* (John Wiley & Sons, New York, 2008).
- [38] J. Egerer, Open source electricity model for germany (ELMOD-DE), Technical Report No. 83, Deutsches Institut für Wirtschaftsforschung, Berlin, 2016.
- [39] M. Rohden, A. Sorge, D. Witthaut, and M. Timme, *Chaos* **24**, 013123 (2014).
- [40] S. Lozano, L. Buzna, and A. Díaz-Guilera, *Eur. Phys. J. B* **85**, 231 (2012).
- [41] S. Olmi, A. Navas, S. Boccaletti, and A. Torcini, *Phys. Rev. E* **90**, 042905 (2014).
- [42] S. Olmi and A. Torcini, in *Control of Self-Organizing Nonlinear Systems*, edited by E. Schöll, S. H. L. Klapp, and P. Hövel (Springer International Publishing, Cham, 2016), Chap. 2, pp. 25–45.
- [43] L. Tumash, S. Olmi, and E. Schöll, *Europhys. Lett.* **123**, 20001 (2018).
- [44] G. Benettin, L. Galgani, A. Giorgilli, and J.-M. Strelcyn, *Meccanica* **15**, 9 (1980).
- [45] P. Kundur, N. J. Balu, and M. G. Lauby, *Power System Stability and Control* (McGraw-Hill, New York, 1994).
- [46] H. Okuno and M. Kawakita, *Electr. Eng. Jpn.* **156**, 7 (2006).
- [47] E. D. Dongmo, P. Colet, and P. Wofo, *Eur. Phys. J. B* **90**, 6 (2017).

- [48] Y. G. Rebours, D. S. Kirschen, M. Trotignon, and S. Rossignol, *IEEE Trans. Power Syst.* **22**, 350 (2007).
- [49] It is important to notice that we do not explicitly perturb the system, but we consider a partially synchronized state naturally coexisting with the synchronized one due to the hysteretic nature of the synchronization transition.
- [50] The different values for the system with bimodal Gaussian distribution $P^G(\alpha = 5/6 \text{ s}^{-1})$ and real-world distribution $P^R(\alpha = 2 \text{ s}^{-1})$ are chosen in order to find unstable, partially synchronized states at comparable coupling strengths, $K = 817 \text{ MW}$ and $K = 729 \text{ MW}$, respectively.
- [51] S. Olmi, *Chaos* **25**, 123125 (2015).
- [52] L. V. Gambuzza, A. Buscarino, L. Fortuna, M. Porfiri, and M. Frasca, *IEEE J. Emerg. Select. Top. Circ. Syst.* **7**, 413 (2017).
- [53] M. Tyloo, L. Pagnier, and P. Jacquod, *Sci. Adv.* **5**, eaaw8359 (2019).
- [54] The map of the Italian high-voltage power grid is shown on the website of the Global Energy Network Institute (<http://www.geni.org>) and the data employed here have been extracted from the map delivered by the union for the co-ordination of transport of electricity(ucte) (<https://www.entsoe.eu/resources/grid-map/>).